

# Ge-based Clinopyroxene series: first principles and experimental local probe study

Ricardo P. Moreira,<sup>1</sup> E. Lora da Silva,<sup>1,2</sup> Gonalo N. P. Oliveira,<sup>1</sup> Pedro Rocha-Rodrigues,<sup>1</sup>  
Alessandro Stroppa,<sup>3</sup> Claire V. Colin,<sup>4</sup> Céline Darie,<sup>4</sup> João G. Correia,<sup>5</sup>  
Lucy V. C. Assali,<sup>6</sup> Helena M. Petrilli,<sup>6</sup> Armandina M. L. Lopes,<sup>1</sup> and João P. Araújo<sup>1,\*</sup>

<sup>1</sup>*IFIMUP, Institute of Physics for Advanced Materials, Nanotechnology and Photonics,  
Departamento de Física e Astronomia da Faculdade de Ciências da Universidade do Porto,  
Rua do Campo Alegre s/n, 4169-007 Porto, Portugal.*

<sup>2</sup>*High Performance Computing Chair, University of Évora,  
Largo dos Colegiais 2, 7004-516 Évora, Portugal*

<sup>3</sup>*CNR-SPIN c/o Università degli Studi dell'Aquila, Via Vetoio 10, 67010 Coppito, L'Aquila, Italy.*

<sup>4</sup>*Université Grenoble Alpes, CNRS, Institut Néel, 38000, Grenoble, France*

<sup>5</sup>*C2TN, DECN, Instituto Superior Técnico, Universidade de Lisboa, Bobadela, Portugal.*

<sup>6</sup>*Instituto de Física, Universidade de São Paulo, CP 66318, 05315-970, São Paulo-SP, Brazil  
(Dated: August 1, 2024)*

The structural and electronic properties of the  $\text{CaMnGe}_2\text{O}_6$  and  $\text{SrMnGe}_2\text{O}_6$  clinopyroxene systems have been investigated by means of perturbed angular correlation (PAC) measurements, performed at ISOLDE, combined with *ab initio* electronic structure calculations within the density functional theory (DFT) framework. The partial density of states (PDOS) of the  $\text{CaMnGe}_2\text{O}_6$  and  $\text{SrMnGe}_2\text{O}_6$  stable compounds has been determined, and it has been observed that the requirement of including an on-site Hubbard- $U$  potential was necessary in order to describe the highly correlated Mn  $3d$ -states. By considering  $U_{\text{eff}}=4$  eV, we obtained a band gap width of 1.82 eV and 1.70 eV, for the  $\text{CaMnGe}_2\text{O}_6$  and  $\text{SrMnGe}_2\text{O}_6$ , respectively. Combining electric field gradient (EFG) first principles calculations, using a supercell scheme, with experimental PAC results, we were able to infer that the Cd probe can replace either the  $A$  (Ca, Sr) or the Mn sites in the crystalline structures. We also showed that Cd substitution is expected to lead to a reduction in the width of the band gap in these systems, evidencing opportunities for potential band-gap engineering.

## I. INTRODUCTION

Pyroxenes are a class of materials with general formula  $AMX_2O_6$ , where  $A$  is a monovalent or a divalent cation,  $M$  is respectively a trivalent or a divalent cation, and  $X$  is typically either Si or Ge. They are well known in mineralogy and geology as they are one of the main rock-forming minerals of the Earth's crust [1]. Within this rich family of compounds, monoclinic pyroxenes (clinopyroxenes), with a  $3d$  transition metal at the  $M$ -site, have recently been the subject of interest in the field of condensed matter physics due to the diversity of their magnetic properties, namely: multiferroicity in  $\text{SrMnGe}_2\text{O}_6$  [2, 3] and  $\text{NaFe}(\text{Si}/\text{Ge})_2\text{O}_6$  [4, 5]; magnetoelectric effect in  $\text{CaMnGe}_2\text{O}_6$  [6] and  $\text{Li}(\text{Cr}/\text{Fe})\text{Si}_2\text{O}_6$  [4]; and also ferrotoroidal ordering in  $\text{LiFeSi}_2\text{O}_6$ .

In spite of their natural prevalence, pyroxenes have not been the subject of much computational or theoretical investigations. It is noteworthy of mentioning, that recent density functional theory (DFT) studies have shown that substitution of  $\text{Al}^{3+}$  by  $\text{Ti}^{3+}$  in  $\text{NaAlSi}_2\text{O}_6$  results in a reduction in the band gap width from 5.32 eV to 2.05 eV. A further reduction is observed when replacing Na by the organic cation  $\text{CH}_3\text{SH}_2$ , showing the high tunability of the band gap in these materials[7]. Other works have shown their potential usefulness in batteries, demonstrating that pyroxenes  $\text{CaFe}/\text{Mn}/\text{Si}_2\text{O}_6$

could display high theoretical energy densities in Ca-based batteries[8], whereas  $\text{LiFeSi}_2\text{O}_6$  has been shown to undergo a reversible electrochemical reaction against Li, thus exhibiting potential for use as an electrode material in Li-ion batteries[9]. Lastly, the magnetic properties of  $\text{CaMnGe}_2\text{O}_6$  were studied by Temnikov *et al.* [10] who computed the exchange parameters and showed that the magnetic frustration in the system is weak, which could explain the frequent occurrence of commensurate collinear antiferromagnetic structures in  $\text{Ca}^{2+}$ -bearing pyroxenes.

The ground state structure for the clinopyroxenes considered in this study is a monoclinic Bravais lattice with space group  $\text{C2}/c$  (#15), where the  $M$ -cations are in octahedral sites (Wyckoff 4e atomic positions), the  $A$ -cations are in 8-coordinated sites (Wyckoff 4e atomic positions) and the  $X$ -cations are in tetrahedral sites (Wyckoff 8f atomic positions). Their structure is characterised by quasi-one-dimensional chains with edge-sharing  $\text{MO}_6$  octahedra running along the  $c$ -axis, and connected by corner-sharing  $\text{XO}_4$  tetrahedra, along the  $c$ -axis, as schematically represented in Fig.1.

When the  $M$ -site is occupied by a magnetic cation, such an arrangement leads to low-dimensional magnetic properties and to magnetic frustration, due to the competition between interchain and intrachain interactions [4]. It is the existence and the possible interplay between the low dimensionality and frustration that is thought to give rise to the aforementioned diversity of magnetic properties in these materials [6]. Moreover, it has been sug-

\* jearaujo@fc.up.pt

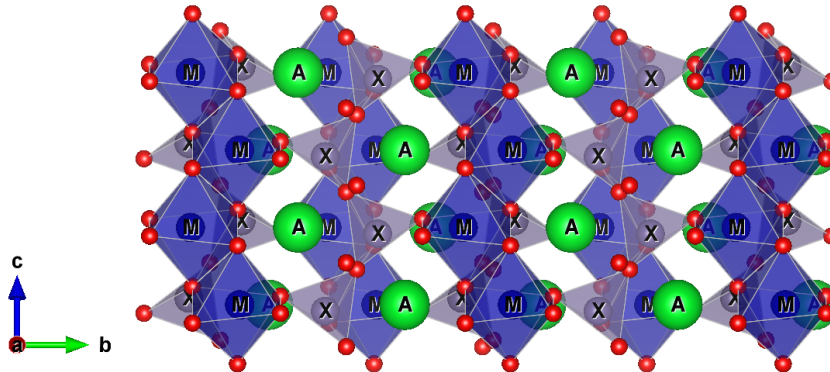


Figure 1. Representation of the  $AMX_2O_6$  clinopyroxene structure. Red spheres represent the oxygen site, green spheres the A-site, grey tetrahedra the X-site coordination polyhedra, and blue octahedra the M-site coordination polyhedra.

gested that the magnetic frustration can lead to spiral spin structures, which may be favourable towards magnetically driven ferroelectricity, making these compounds good candidates for multiferroic behaviour [4]. Since these properties are thought to arise from local features that are often not accurately described by long-range order based techniques, such as X-ray diffraction and Raman spectroscopy, it is important to utilise techniques that are more sensitive to local order to aid in the characterisation of these intriguing systems. Several works have, in the past, studied pyroxene systems by means of nuclear techniques, such as nuclear magnetic resonance spectroscopy [11–13] and Mössbauer spectroscopy [14–16]; however, and to the best of the authors’ knowledge, this is the first work being reported where the pyroxene systems are studied via perturbed angular correlation (PAC) spectroscopy. In particular, none of the nuclear techniques above mentioned have been used to characterise the systems here under study.

In the present work, the  $AMnGe_2O_6$  germanate clinopyroxene series were explored, where the A-site is occupied by periodic table group-II elements, i.e., Be, Mg, Ca, and Sr. The former two compounds have so far not been experimentally realised, and they were thus studied solely through *ab initio* calculations.  $(Ca,Sr)_{1-x}Cd_xMnGe_2O_6$  and  $(Ca,Sr)Mn_{1-x}Cd_xGe_2O_6$  were explored by means of *ab initio* computational simulations, from which we were able to estimate the band gaps, as well as the effective masses of the electrons and holes of the systems; and by local Cd probe experiments using PAC spectroscopy, allowing one to closely follow the temperature evolution of the electric field gradient (EFG) tensor.

## II. METHODS

### A. Experimental Methods

For the purpose of performing the PAC measurements, pelletised samples of  $CaMnGe_2O_6$  and  $SrMnGe_2O_6$  materials were implanted at ISOLDE-CERN by a 30 keV beam of  $^{111m}Cd$  probes [ $^{111m}Cd \rightarrow ^{111}Cd$ ,  $t_{1/2} = 48.6$  minutes], which have a nuclear spin  $I = 5/2$  and an electric quadrupole moment of  $Q = 0.83(13)$  b in the intermediate state of decay [17]. Small doses of the order of  $10^{11}$  atoms/cm<sup>2</sup> were implanted and subsequently an annealing was performed at a temperature of  $\sim 1123$  K for 20 minutes in air to recover from implantation damage. Confirmation for the recovery of point defects and for the incorporation of Cd into the lattice was given by the PAC measurements themselves, which yielded well-defined experimental  $R(t)$  anisotropy functions. The measurements were performed on 6-BaF<sub>2</sub> detectors PAC spectrometers [18], equipped with either a closed-cycle refrigerator or a special high-temperature furnace for temperature control. Due to the relatively short lifetime of the parent probe, each temperature point required the implantation of a new sample for satisfactory activity to be maintained during measurement. The experimental  $R(t)$  function was fitted with exact numerical methods that build the expected observable by solving the hyperfine interaction Hamiltonian’s characteristic equations [19–23]. The EFG, that characterizes the surrounding charge density that interacts with a probe nucleus, can be represented as a rank-2 symmetric and traceless tensor. As such it is always possible to diagonalise it by rotating the axis system into the EFG eigenbasis, that is referred to as the principal reference frame. The experimentally observable EFG is conventionally de-

scribed by two parameters, the principal component  $V_{zz}$  and the axial asymmetry parameter:

$$\eta = \frac{V_{xx} - V_{yy}}{V_{zz}}, \quad (1)$$

with  $V_{zz}$ ,  $V_{yy}$  and  $V_{xx}$  being the eigenvalues of the EFG tensor, defined such that  $|V_{zz}| \geq |V_{yy}| \geq |V_{xx}|$  [19].

The signature for the interaction between the probe atoms and their local environment is the perturbation function  $G_{kk}(t)$ . In the case of static electric quadrupole interactions, the interaction can be written as [24]:

$$G_{kk}(t) = \sum_n s_{k_n} \cos(\omega_n t) e^{-\delta \omega_n t/2}, \quad (2)$$

where  $s_{k_n}$  and  $\omega_n$  are functions of  $\eta$  and the fundamental frequency  $\omega_Q$ . The exponential term arises from randomly distributed vacancies, defects, and lattice strains that result in an attenuation of the experimental  $R(t)$  function. In the case of the  $^{111}\text{mCd}$  probes, the intermediate level in the decay has a nuclear spin of  $I = 5/2$ , which leads to a split of the intermediate level into three sub-levels due to the quadrupole interaction and three transition frequencies,  $\omega_1$ ,  $\omega_2$ , and  $\omega_3 = \omega_1 + \omega_2$ . The fundamental frequency is usually defined as [19]:

$$\omega_Q = \frac{eQV_{zz}}{4I(2I-1)\hbar}, \quad (3)$$

where  $Q$  is the nuclear quadrupole moment,  $e$  is the electron charge, and  $\hbar$  is the reduced Planck constant.

## B. Computational Methodology

DFT calculations were performed by using the Quantum Espresso (QE) [25, 26] suite with Projector-Augmented Wave (PAW) datasets [27, 28]. The atomic valence configurations that were considered for the calculations were: Be[2s<sup>2</sup>], Ca[3s<sup>2</sup>3p<sup>6</sup>4s<sup>2</sup>], Cd[4d<sup>9.5</sup>5s<sup>2</sup>5p<sup>0.5</sup>], Ge[3d<sup>10</sup>4s<sup>2</sup>4p<sup>2</sup>], Mg[2s<sup>2</sup>2p<sup>6</sup>3s<sup>2</sup>], Mn[3s<sup>2</sup>3p<sup>6</sup>3d<sup>5</sup>4s<sup>2</sup>], O[2s<sup>2</sup>2p<sup>4</sup>], and Sr[4s<sup>2</sup>4p<sup>6</sup>5s<sup>2</sup>]. The kinetic energy cutoffs were converged to the values of 70 and 540 Ry for the wavefunctions and the charge density, respectively. However, in order to converge the EFGs to the experimental data, and for the calculations that included the Cd substitutional atom, these values were raised to 113 and 900 Ry, for the wavefunctions and the charge density, respectively. Regarding the exchange-correlation (XC) functional, the generalised gradient approximation (GGA) with Perdew-Burke-Ernzerhof [29] (PBE) parametrization was employed. In order to treat the strongly correlated *3d*-states of Mn, an effective Hubbard- $U$  potential was considered by defining  $U_{eff} = 4$  eV [30, 31], by employing the simplified version of Cococcioni and de Gironcoli [32], with PBE (PBE+ $U$ ).

In order to obtain the ground-state properties, total energy minimization with respect to the changes in the

atomic positions and cell parameters were taken into account, until the total force did not exceed 0.05 eV/Å, and constraining the system to zero internal pressure, with the variable cell shape relaxation, considering the damped Beeman ionic dynamics and the Wentzcovitch extended Lagrangian for the cell dynamics [33–35]. For the four compounds, the enthalpies of formation were determined by comparing respective total energies to that of the respective DFT total energy of the  $\text{AGeO}_3$  and  $\text{MnGeO}_3$  stable constituent oxides (Eq. A1 in Appendix A). With respect to the  $\text{CaMnGe}_2\text{O}_6$  and  $\text{SrMnGe}_2\text{O}_6$  compounds, the EFGs were evaluated for the pristine unit-cell, as well as for the unit-cell and the  $1 \times 1 \times 2$  supercell by considering Cd substitution of either A or Mn cation sites (Fig. 2), in order to compare with previously obtained PAC measurements. The computation of the EFGs was performed by using the Gauge Including Projector Augmented Waves (GIPAW) [36] package routine implemented in QE.

For the supercell calculations, only the atomic positions were relaxed, by using the lattice parameters obtained from the pristine unit-cell structural minimization (by employing the variable cell shape relaxations). The Brillouin-zones (BZ) were sampled with a  $(9 \times 9 \times 18)$  Monkhorst-Pack  $\mathbf{k}$ -point grids for unit-cell calculations, and a  $(9 \times 9 \times 9)$  for calculations on the  $1 \times 1 \times 2$  supercells; whereas for the calculation of EFGs and PDOS,  $\mathbf{k}$ -point grids of  $(11 \times 11 \times 22)$  and  $(11 \times 11 \times 11)$  were used, for the unit-cells and supercells, respectively.

## III. RESULTS AND DISCUSSION

### A. Perturbed Angular Correlation

The PAC measurements on the  $\text{SrMnGe}_2\text{O}_6$  (SMGO) system were performed at selected temperatures in the 13-902 K range. Figure 3 shows a few representative experimental  $\gamma-\gamma$   $R(t)$  perturbation functions obtained for the  $\text{SrMnGe}_2\text{O}_6$  compound along with their corresponding Fourier transforms. Several models were tested in order to numerically obtain the best fit to the experimental  $R(t)$  spectra before arriving at the presented model, wherein two distinct fractions (two distinct local environments) are evident across the whole temperature range, indicating the probes interacted with two distinct EFG distributions, henceforth referred to as  $\text{EFG}^{\text{SMGO}_1}$  and  $\text{EFG}^{\text{SMGO}_2}$ , and represented by the green and blue lines in figure 3, respectively.

The temperature behaviour of the experimental  $R(t)$  fit parameters of SMGO is displayed in figure 4. One can observe, in figure 4 a), green circles, that the  $V_{zz}$  value for the  $\text{EFG}^{\text{SMGO}_1}$  fraction has a noticeable increase at low temperatures, with increasing temperature, reaching a maximum; whereupon it starts to decrease. On the other hand, the axial asymmetry  $\eta(1)$  parameter increases as the temperature increases, as displayed in figure 4 b) by the green circles. The EFG aforementioned behaviour is

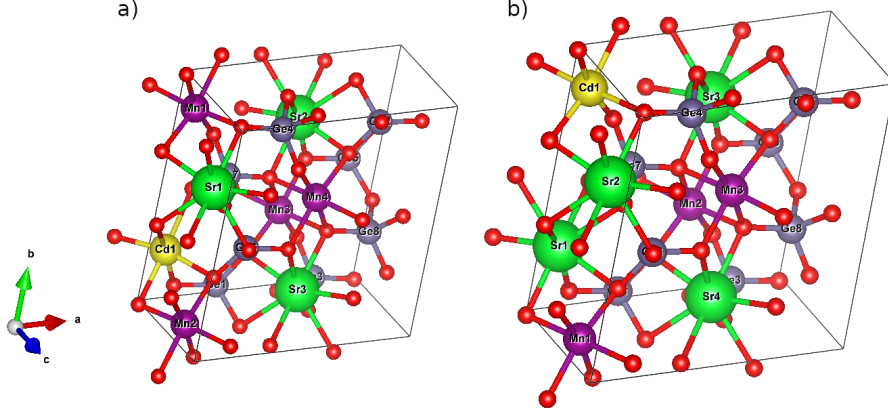


Figure 2. Representation of the  $AMX_2O_6$  clinopyroxene structure. Red spheres represent the oxygen site, green spheres the A-site, grey tetrahedra the X-site coordination polyhedra, and blue octahedra the M-site coordination polyhedra.

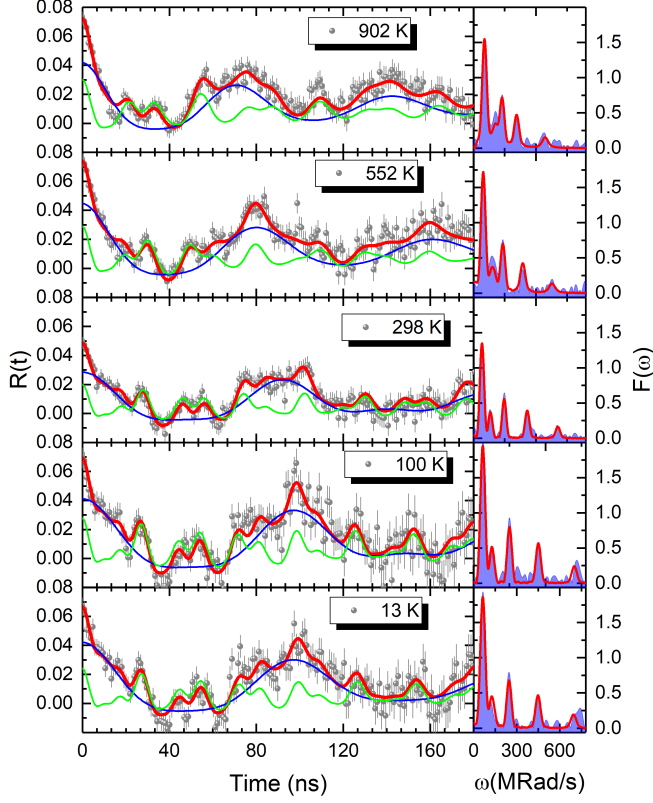


Figure 3. Representative  $R(t)$  spectra of  $SrMnGe_2O_6$  and corresponding fits (left), as well as Fourier transforms (right).

typical for a phonon contribution to  $V_{zz}$  and, accordingly, a temperature dependence least-squares fit by the Bayer-Kushida[37–39] model, with a single phonon frequency, was done, according to

$$V_{zz}(T) = V_{zz}(0) \left\{ 1 - \frac{3}{8\pi^2} \frac{hA}{\nu} \left( \frac{1}{2} + \frac{1}{e^{\frac{h\nu}{kT}} - 1} \right) \right\}, \quad (4)$$

where  $h$  is the Planck constant,  $\nu$  is the phonon fre-

quency,  $k$  is the Boltzmann constant and  $A$  is a quantity that in general can only be said to have the dimensions and order of magnitude of the inverse of the moment of inertia associated to the molecular vibration, except in specific cases where it is indeed the inverse of the moment of inertia associated with a normal mode of molecular vibration[39]. From this fitting, we have obtained  $\nu = 8.01(7) \times 10^{12}$  Hz, which is within the range of frequencies that are typical for intra-molecular vibrations and is comparable to the value of  $6.60(85) \times 10^{12}$  Hz reported for  $Ca_2MnO_4$ [40], suggesting that the  $V_{zz}$  temperature behaviour for the  $EFG^{SMGO_1}$  local environment is indeed due to a phonon contribution. Regarding the axial asymmetry parameter  $\eta(1)$  at the  $EFG^{SMGO_1}$  site, it displays an intermediate asymmetry, which increases as temperature raises.

For the  $EFG^{SMGO_2}$  fraction, depicted by the blue triangles in figure 4 a), the  $V_{zz}$  shows an atypical behaviour of increasing as temperature also increases, though such behaviour has nevertheless been reported in other compounds. Specifically, analogous behaviour was experimentally observed in the  $A2_1am$  phase of  $Ca_3Mn_2O_7$  for which DFT simulations indicated that such behaviour is actually due to structural effects, that prevail over the phonon contributions [41]. The asymmetry parameter  $\eta(2)$  for the  $EFG^{SMGO_2}$  fraction, as displayed in figure 4 b) by the blue triangles, on the other hand, remains approximately constant, up to 474 K, whereupon an anomalous increase occurs. It is unclear if such behaviour could be related to structural phenomena, as there are no measurements reported for temperatures above 350 K. It is worth noting that the probes distribution between both fraction remained fairly constant across the whole temperature range, suggesting that they are related to the probes occupying two distinct lattice sites.

With respect to the  $CaMnGe_2O_6$  (CMGO) system, the PAC measurements were likewise performed at selected temperatures, in the 11-898 K range. Representative fits to the experimental  $R(t)$  perturbation func-



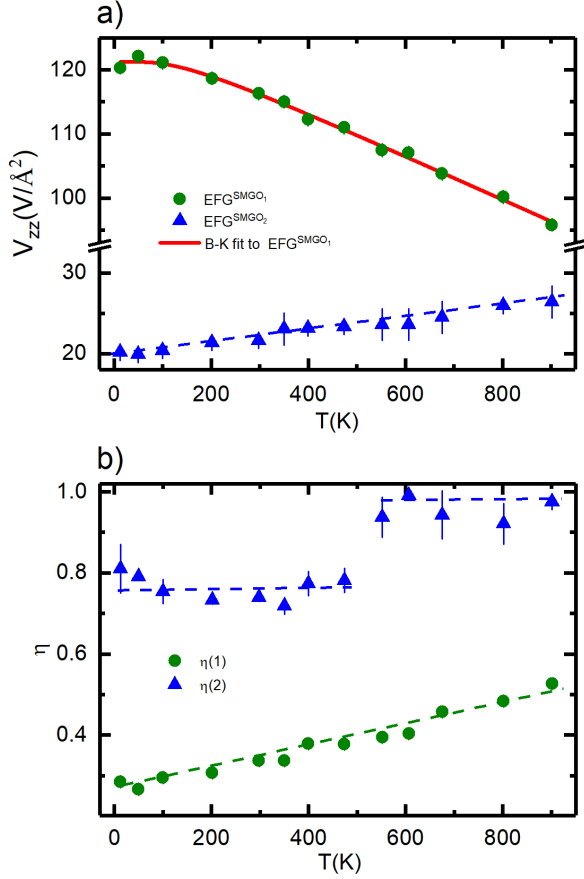


Figure 4. a) Experimental  $V_{zz}$  for  $\text{SrMnGe}_2\text{O}_6$ ; b) Experimental axial asymmetry for  $\text{SrMnGe}_2\text{O}_6$ . The green circles correspond to  $\text{EFG}^{\text{SMGO}_1}$  fraction and blue triangles to  $\text{EFG}^{\text{SMGO}_2}$  fraction. The full red line corresponds to a fit of the temperature dependence of  $V_{zz}^{\text{SMGO}_1}$  by the Bayer-Kushida model [37–39], while the dashed lines are merely a guide to the eye.

tions for CMGO are presented in figure 5, along with the corresponding Fourier transforms. Similar to how the data from the previous compound was treated, several models were also tested in order to numerically obtain the best fit to the experimental  $R(t)$  spectra. Distinctly from  $\text{SrMnGe}_2\text{O}_6$ , wherein two noticeable fractions are present across the whole temperature range, for the  $\text{CaMnGe}_2\text{O}_6$  compound there is only one fraction present from low temperatures, up to 351 K, hereby referred to as  $\text{EFG}^{\text{CMGO}_1}$  and represented by the green lines in figure 5. It can be noticed in this figure that a second fraction, labeled  $\text{EFG}^{\text{CMGO}_2}$ , appears for temperatures above 351 K, represented by the blue lines. However, it is likely that this second fraction is likewise present at lower temperatures, but owing to the very small observable frequency associated with it, that is not well defined in the time window available in the PAC experiments, it is not possible to fit this fraction at lower temperatures. Even at high temperatures the  $\text{EFG}^{\text{CMGO}_2}$  fitting parameters have nonetheless an asso-

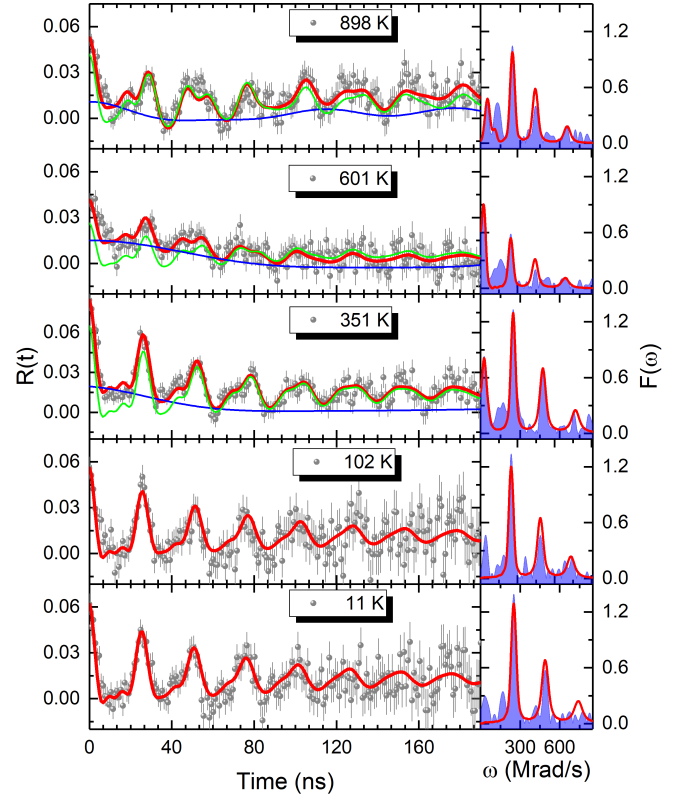


Figure 5. Representative  $R(t)$  spectra of  $\text{CaMnGe}_2\text{O}_6$  and corresponding fits (left), as well as Fourier transforms (right).

ciated high uncertainty.

The temperature behaviour of the fit parameters relative to the  $\text{CaMnGe}_2\text{O}_6$  system are shown in figure 6. One can observe, in figure 6 a), green circles, that the  $\text{EFG}^{\text{CMGO}_1}$  distribution has a  $V_{zz}$  value of similar magnitude to  $\text{EFG}^{\text{SMGO}_1}$  (figure 4 a)), with an analogous decrease as temperature raises.

Also  $\eta(1)$ , displayed in figure 6 b), green circles, similarly increases with increasing temperature, when compared to SMGO  $\eta(1)$  variation (figure 4 b)). As was done in the case of the  $\text{SrMnGe}_2\text{O}_6$  compound, a least-squares fits was likewise performed to  $V_{zz}$ , according to equation 4. From the fit, a frequency of  $\nu = 10.0(2) \times 10^{12}$  Hz was obtained, once more indicating that this behaviour is likely attributable to a phonon contribution to  $V_{zz}$ . Similarly to what was observed for  $\text{SrMnGe}_2\text{O}_6$ , we note that the magnetic hyperfine interactions were not apparent in the fits to the experimental  $R(t)$  functions.

## B. Density Functional Theory Calculations

### 1. Structural Parameters

We begin this section by summarizing in Table I the calculated lattice parameters for the  $\text{SrMnGe}_2\text{O}_6$  and  $\text{CaMnGe}_2\text{O}_6$  systems, computed by applying both the

Table I. Experimental [2, 6] and theoretical lattice parameters for  $\text{SrMnGe}_2\text{O}_6$  and  $\text{CaMnGe}_2\text{O}_6$  compounds, obtained by using the PBE XC functional, without and with an effective Hubbard- $U$  potential correction to describe the strongly correlated Mn 3d-states, labeled as PBE and PBE+ $U$ , respectively.

System	Research type	$a$ (Å)	$b$ (Å)	$c$ (Å)	$\beta$ (°)
$\text{SrMnGe}_2\text{O}_6$	Expt.	10.3511(6)	9.4204(5)	5.5093(3)	104.700(2)
	Theo. PBE	10.5295	9.4912	5.5992	105.029
	Theo. PBE+ $U$	10.5638	9.5795	5.6230	104.906
$\text{CaMnGe}_2\text{O}_6$	Expt.	10.2794(3)	9.1756(3)	5.4714(2)	104.244(2)
	Theo. PBE	10.4006	9.2248	5.5194	103.921
	Theo. PBE+ $U$	10.4495	9.3204	5.5472	104.109

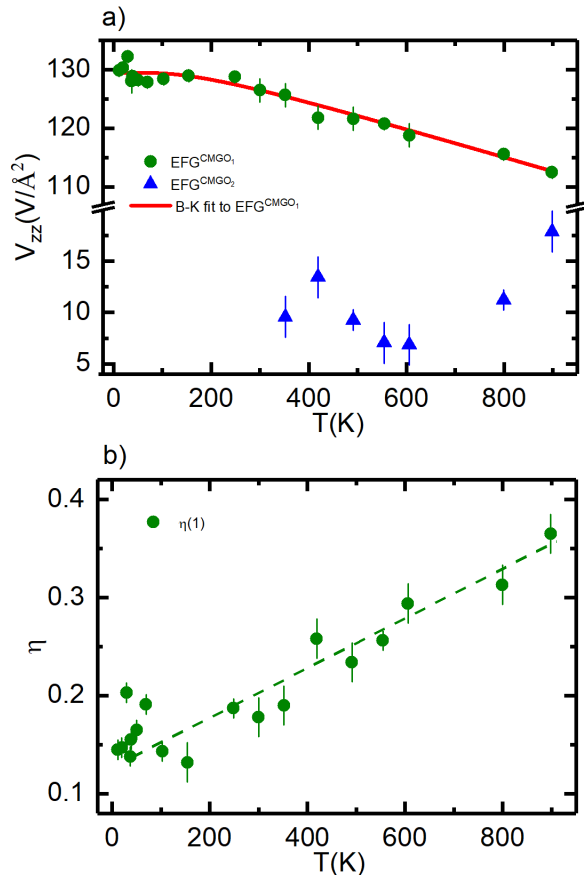


Figure 6. a): Experimental  $V_{zz}$  for  $\text{CaMnGe}_2\text{O}_6$ . b): Experimental axial asymmetry  $\eta$  for  $\text{CaMnGe}_2\text{O}_6$ . The green circles correspond to EFG<sup>CMGO<sub>1</sub></sup> fraction and blue triangles to EFG<sup>CMGO<sub>2</sub></sup> fraction. The continuous red line corresponds to a fit of the temperature dependence of  $V_{zz}^{\text{CMGO}_1}$  by the Bayer-Kushida model[37–39], while the dashed lines are merely meant to guide the eye.

PBE and PBE+ $U$  methodologies, as well as the reported experimental values,[2, 6] for comparison purposes.

Regarding the  $\text{SrMnGe}_2\text{O}_6$  system, we can observe that the lattice parameters computed with the PBE functional are overestimated, with respect to the experimental values, corresponding to a relative increase of  $\sim 1.7\%$ ,

$\sim 0.8\%$ , and  $\sim 1.6\%$ , respectively, for  $a$ ,  $b$ , and  $c$  parameters, which is in line with the well-known tendency of the PBE functional.[42] The inclusion of the on-site effective Hubbard- $U$  potential results in a further relative increase of these parameters with  $\sim 2.1\%$ ,  $\sim 1.7\%$ , and  $\sim 2.1\%$ , when compared to the experimental values. Though the  $\beta$  monoclinic angle is overestimated for both PBE and PBE+ $U$  approximations, when comparing to experimental data, the difference is in fact smaller when considering the PBE+ $U$  calculations, resulting in a value closer to the experimental one.

With respect to  $\text{CaMnGe}_2\text{O}_6$ , the  $a$  and  $b$  theoretical lattice parameters obtained from PBE calculations likewise are overestimated, relative to experimental data, by  $\sim 1.2\%$  and  $\sim 0.5\%$ , respectively. On the other hand we observed that the  $c$  parameter is underestimated by  $\sim 0.9\%$ . Analogously to what was observed for  $\text{SrMnGe}_2\text{O}_6$ , the  $a$  and  $b$  lattice parameters that resulted from the PBE+ $U$  approach display an increase with respect to the PBE values, presenting an overestimation of  $\sim 1.7\%$  and  $\sim 1.6\%$ , respectively, with respect to experimental results; whereas  $c$  parameter is still underestimated, though smaller than the one obtained by the PBE functional, of  $\sim 0.4\%$ . Also, and distinctly from what was observed for  $\text{SrMnGe}_2\text{O}_6$ , the theoretical monoclinic angle is underestimated relative to the experimental angle, though again, results from the PBE+ $U$  approximation is closer to the experimental value.

## 2. Enthalpies of Formation

The enthalpy of formation of the constituent oxides of the  $\text{AMnGe}_2\text{O}_6$  series has also been examined through DFT calculations and we have determined that only the  $\text{CaMnGe}_2\text{O}_6$  and  $\text{SrMnGe}_2\text{O}_6$  clinopyroxene compounds are thermodynamically stable. This is evidenced by their negative enthalpies of formation of  $-0.19$  eV/f.u. and  $-0.11$  eV/f.u., respectively (calculated by considering equation A1 of Appendix A). On the other hand, the  $\text{BeMnGe}_2\text{O}_6$  and  $\text{MgMnGe}_2\text{O}_6$  systems both evidenced positive enthalpies of formation of  $0.12$  eV/f.u., supporting that these are not stable against dissociation into the respective stable constituent oxides  $\text{BeGeO}_3$  or  $\text{MgGeO}_3$  and  $\text{MnGeO}_3$ . This observation is consistent with the

fact that only the former two compounds have been experimentally synthesised, whereas the synthesis of the latter two has not yet been reported. Such observation implies that different reaction pathways towards synthesis will have to be explored if these systems were to be experimentally realised. Details on how the enthalpies of formation were obtained are presented in the Appendix A.

### 3. Partial Density of States

The PDOS for the  $\text{CaMnGe}_2\text{O}_6$  and  $\text{SrMnGe}_2\text{O}_6$  compounds, obtained considering the PBE calculation, without the Hubbard- $U$  correction ( $U_{\text{eff}} = 0$  eV), were computed and are displayed in figure 7, in which the valence band maximum (VBM) is aligned at the Fermi energy and is set to zero. Two narrow bands form the VBM, and these are mainly composed by the Mn occupied  $3d$ -states, hybridized with a smaller contribution from the O  $p$ -states. Energetically below these narrow bands ( $< -2.5$  eV), a broader band is observed and it is mostly dominated by the O  $p$ -states, with a small mixture of  $3d$ -states from Mn. The conduction band minimum (CBM), on the other hand, presents low density of states and hybridization between the  $p$ -states of O and Ge. For increasing energies, the DOS significantly increases forming a narrow resonant band, between 2.5 and 3.0 eV, that is mainly composed by the Mn  $3d$ -states unoccupied states.

For both studied systems the PDOS are qualitatively very similar, although at the conduction band the observed resonant peaks of Mn for  $\text{SrMnGe}_2\text{O}_6$  are much broader when compared to those of  $\text{CaMnGe}_2\text{O}_6$ .

The electronic band gaps are also noted to be fairly narrow, being 0.46 eV and 0.51 eV, respectively, for  $\text{CaMnGe}_2\text{O}_6$  and  $\text{SrMnGe}_2\text{O}_6$ , which is narrower than what has been reported for similar Si-based compounds[7, 43].

Since the band gap widths are likely underestimated in the absence of the Hubbard- $U$  correction, we have also considered the PDOS by including the  $U_{\text{eff}} = 4$  eV, applied to the Mn  $3d$ -states. These are shown in figure 9 along with the respective electronic band structures in the high-symmetry directions of the primitive cell first Brillouin zone (figure 8).

When including the  $U_{\text{eff}} = 4$  eV, and comparing to the PDOS results when  $U_{\text{eff}} = 0$  eV, differences are mainly evidenced at the VBM, with the Mn  $3d$ -states. The two narrow bands observed in figure 7, now overlap and form one narrow band for  $\text{CaMnGe}_2\text{O}_6$  (figure 9 a)). As for the  $\text{SrMnGe}_2\text{O}_6$  system, the narrow bands are energetically very close, almost forming also one narrow band (figure 9 b)). Moreover, these narrow bands are now dominated by a stronger hybridization between Mn  $d$ -states with the O  $p$ -states.

Since the inclusion of the  $U$  parameter localises and positions the unoccupied narrow  $3d$ -states of Mn higher in energy (between 5.0 and 5.5 eV), the CBM shows

slightly increased  $p$  hybridized states of O and Ge, than when  $U$  is not considered. The PBE+ $U$  theoretical band gaps are now wider, when compared to the previous case, with 1.82 eV and 1.70 eV for the  $\text{CaMnGe}_2\text{O}_6$  and  $\text{SrMnGe}_2\text{O}_6$  compounds, respectively. Despite this, the gap widths are still below the range of other similar Si-based clinopyroxenes[7, 43].

### 4. Electronic Bandstructures

The electronic bandstructures for the pristine  $\text{CaMnGe}_2\text{O}_6$  and  $\text{SrMnGe}_2\text{O}_6$  systems, as well as the respective Cd-containing supercells were also computed through DFT calculations, in a path along the high-symmetry points depicted in figure 8, generated with the SeeK-path tool.[44, 45]

The bandstructures for the pristine systems are presented in figure 9, whilst those for the supercells can be found in Appendix C.

Differences between both pristine systems is evidenced by the character of the band gap: while  $\text{SrMnGe}_2\text{O}_6$  exhibits a direct band gap,  $\text{CaMnGe}_2\text{O}_6$  has an indirect gap. We must stress that subtleties persist with respect to the analysis of the VBM, since the valence bands are quite flat, and thus the electronic bands along the different high symmetry segments/points are energetically very close.

From figure 9, one can observe that the top of the valence band is much flatter than the bottom of the conduction band, which shows narrow parabolas around the zone-centre, indicating that the effective mass of the holes,  $m_h^*$ , is much larger than the effective mass of electrons,  $m_e^*$ . Such an observation is an indication of a higher mobility of the electrons comparatively to the holes of the system. Since the effective mass of the charge carriers is an essential parameter for the performance of photoelectric and photo-catalytic activities[46], and also for semiconductor radiation detectors[47]; we have considered further analysing respective properties (table II). Therefore and to quantify the effective masses of holes and electrons, we employ the well-known definition of the effective mass as

$$m^* = \frac{\hbar^2}{\frac{\partial^2 E}{\partial k^2}}, \quad (5)$$

with the second derivative of the electronic dispersion relation being obtained from a quadratic fit around the energy range where the band edges are located.

In the case of  $\text{CaMnGe}_2\text{O}_6$ , we obtain a  $m_e^*$ , around the  $\Gamma$ -point, very close to that of the free electrons, with  $m_e^* = 1.028m_0$  (where  $m_0$  is the mass of the free electron with  $9.11 \times 10^{-31}$  kg). While for the hole carriers, and as expected by considering the flatness-shape of the VBM, the mass of holes proved to be substantially larger (in absolute terms) with  $m_h^* = 26.125m_0$ , and calculated along the high-symmetry segment of  $\overline{A}\Gamma \rightarrow A$  (table II).

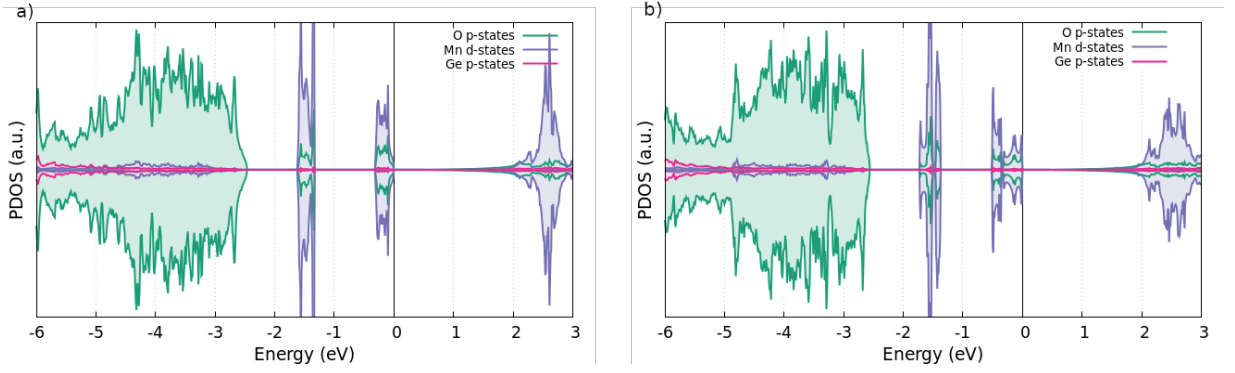


Figure 7. Partial density of states of (a)  $\text{CaMnGe}_2\text{O}_6$  and (b)  $\text{SrMnGe}_2\text{O}_6$ , computed with  $U_{\text{eff}} = 0$  eV, and considering antiferromagnetic ordering. The Fermi level is set to zero and corresponds to the VBM.

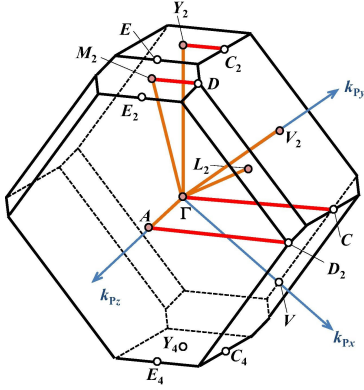


Figure 8. First Brillouin zone of the base-centered monoclinic lattice and respective high-symmetry points and directions. Adapted from reference 44.

Regarding the Cd-containing supercells of  $\text{CaMnGe}_2\text{O}_6$ , when Cd substitution was considered at the Ca site, we found that the effective masses of the electrons only yielded mild variation when compared to the pristine system. For the electrons, the  $m_e^*$  showed very little to no increase with  $m_e^* = 0.996m_0$  and  $m_e^* = 1.028m_0$ , for the  $\text{Ca}_{3/4}\text{Cd}_{1/4}\text{MnGe}_2\text{O}_6$  and  $\text{Ca}_{7/8}\text{Cd}_{1/8}\text{MnGe}_2\text{O}_6$  systems, respectively. In the case of the holes, we observe that for the  $\text{Ca}_{3/4}\text{Cd}_{1/4}\text{MnGe}_2\text{O}_6$  cell, and by comparing to the pristine system,  $m_h^*$  slightly increases along the  $\overline{A\Gamma} \rightarrow \Gamma$  with  $m_h^* = 45.259m_0$ , although showing similar values along  $\overline{A\Gamma} \rightarrow A$  with  $m_h^* = 27.875m_0$ .

With respect to the larger supercell ( $\text{CaMn}_{7/8}\text{Cd}_{1/8}\text{Ge}_2\text{O}_6$ ), we observe a very high increase with respect to the pristine system, with  $m_h^* = 67.562m_0$ , along the same high-symmetry segment.

On the other hand, when the Cd atom was placed at the Mn site, we found that the dopant affected the valence band edge even further, leading to a further flat-tening of the VBM; however, and once again, the  $m_e^*$  remained very similar to the pure unit-cell. A significant increase of the hole effective mass was found for the  $\text{CaMn}_{3/4}\text{Cd}_{1/4}\text{Ge}_2\text{O}_6$  structure ( $V_2 \rightarrow \Gamma$  direction), with

$m_h^* = 118.325m_0$ . Moreover, for the more diluted system we observed that along  $\overline{A\Gamma} \rightarrow A$  the effective mass decreases slightly ( $m_h^* = 28.65m_0$ ), showing an increase of  $m_h^*$  in the direction of  $\overline{A\Gamma} \rightarrow A$  ( $m_h^* = 68.128m_0$ ).

Regarding the pristine  $\text{SrMnGe}_2\text{O}_6$  structure, we found a similar value for the electron effective mass with  $m_e^* = 1.023m_0$ . However, a significantly more parabolic dispersion relation at the VBM when compared to  $\text{CaMnGe}_2\text{O}_6$ , leading to a hole effective mass of  $m_h^* = 9.380m_0$ , when considering the  $\Gamma \rightarrow D$  segment. We must however state that since the valence band dispersion is quite asymmetric, the interpolation with a quadratic function did not yield a very accurate fit to the dispersion relation; therefore the value of the  $m_h^*$  should be understood more as an order of magnitude rather than a quantitative value. Once again, we observe that with the Cd substitution, there is only a mild variation of  $m_e^*$ , leading to a slightly increased value of  $m_e^* = 1.028m_0$  for  $\text{Sr}_{7/8}\text{Cd}_{1/8}\text{MnGe}_2\text{O}_6$ , and a more pronounced increase for the  $\text{Sr}_{3/4}\text{Cd}_{1/4}\text{MnGe}_2\text{O}_6$  compound with  $m_e^* = 1.106m_0$ . As for the  $\text{SrMn}_{3/4}\text{Cd}_{1/4}\text{Ge}_2\text{O}_6$  and  $\text{SrMn}_{7/8}\text{Cd}_{1/8}\text{Ge}_2\text{O}_6$  systems, a slight increase of the effective masses is observed to  $m_e^* = 1.068m_0$  and  $m_e^* = 1.057m_0$ , respectively. With respect to the  $m_h^*$ , we again note that due to the flat-shape of the bands, a parabolic interpolation does not provide a dependable quantitative value, so we can only state with confidence that this value should remain of the same order as that of the pristine  $\text{SrMnGe}_2\text{O}_6$  compound. We must state that such observed differences of the masses between the charge carriers is quite interesting because of the increased possibility to enhance the separation of the electron-hole pairs, and even of evidencing large electron and hole drift lengths[47], thus affecting the optoelectronic properties of the studied clinopyroxenes [48]. The band gaps were also determined for all systems from the bandstructure calculations, and are summarised in Table II. As already observed for the PDOS, the band gaps for all systems lie between 1.70 eV and 1.82 eV for the pristine systems,  $\text{SrMnGe}_2\text{O}_6$  and  $\text{CaMnGe}_2\text{O}_6$ , respectively; whereas the doped structures show narrower



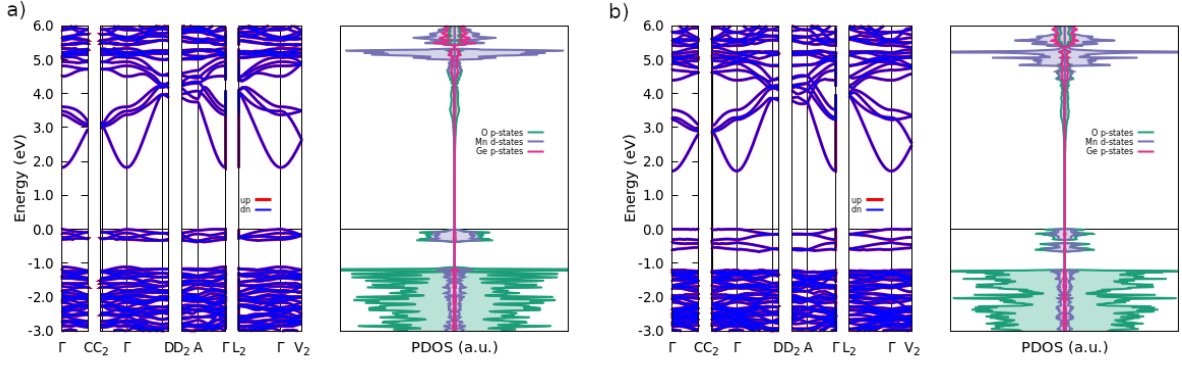


Figure 9. Bandstructures in the high-symmetry directions of the primitive cell first Brillouin zone (figure 8) (left) and partial density of states (right) of a)  $\text{CaMnGe}_2\text{O}_6$  and b)  $\text{SrMnGe}_2\text{O}_6$ , both computed with  $U_{\text{eff}} = 4$  eV to treat the strongly correlated Mn 3d-states, and considering antiferromagnetic ordering. The Fermi level is set to zero and matches the VBM.

Table II. Electronic properties of the studied systems without and with Cd, considered as dopant, and applying  $U_{\text{eff}} = 4$  eV to treat the Mn 3d-states. The values of the effective masses are given in units of the electron mass:  $m_0 = 9.11 \times 10^{-31}$  kg.)

System	Band Character	Band gap (eV)	$m_e^* (m_0)$	$m_h^* (m_0)$
$\text{SrMnGe}_2\text{O}_6$	Direct	1.70	1.023	9.380 ( $\Gamma \rightarrow D$ )
$\text{Sr}_{7/8}\text{Cd}_{1/8}\text{MnGe}_2\text{O}_6$	Indirect	1.55	1.028	58.223 ( $\overline{C}_2\Gamma \rightarrow C_2$ )
$\text{Sr}_{3/4}\text{Cd}_{1/4}\text{MnGe}_2\text{O}_6$	Indirect	1.43	1.106	58.287 ( $\overline{C}_2\Gamma \rightarrow C_2$ )
$\text{SrMn}_{7/8}\text{Cd}_{1/8}\text{Ge}_2\text{O}_6$	Indirect	1.56	1.057	40.062 ( $\overline{C}_2\Gamma \rightarrow C_2$ )
$\text{SrMn}_{3/4}\text{Cd}_{1/4}\text{Ge}_2\text{O}_6$	Indirect	1.50	1.068	46.882 ( $V_2 \rightarrow \Gamma$ )
$\text{CaMnGe}_2\text{O}_6$	Indirect	1.82	1.028	26.125 ( $\overline{A}\Gamma \rightarrow A$ )
$\text{Ca}_{7/8}\text{Cd}_{1/8}\text{MnGe}_2\text{O}_6$	Indirect	1.59	1.028	67.562 ( $\overline{A}\Gamma \rightarrow A$ )
$\text{Ca}_{3/4}\text{Cd}_{1/4}\text{MnGe}_2\text{O}_6$	Indirect	1.42	0.996	27.875 ( $\overline{A}\Gamma \rightarrow A$ ) 45.259 ( $\overline{A}\Gamma \rightarrow \Gamma$ )
$\text{CaMn}_{7/8}\text{Cd}_{1/8}\text{Ge}_2\text{O}_6$	Indirect	1.58	1.033	18.704 ( $\overline{A}\Gamma \rightarrow A$ ) 68.128 ( $\overline{A}\Gamma \rightarrow \Gamma$ )
$\text{CaMn}_{3/4}\text{Cd}_{1/4}\text{Ge}_2\text{O}_6$	Indirect	1.61	1.058	118.325 ( $V_2 \rightarrow \Gamma$ )

band gaps. All the doped structures show indirect band gap character, even for the Sr-based structures, where the pristine counterpart evidences a direct one (figure 9 and figures C1 to C9 in Appendix C).

### 5. Ab Initio Electric Field Gradients

The DFT EFGs calculations were performed for the pristine unit-cells, along with the EFGs for the unit-cells and  $1 \times 1 \times 2$  supercells with Cd substitution, either at the A- or the Mn-sites. Results were compared with those obtained for the experimental EFG fractions and are summarised in Table III, whilst a more com-

prehensive list of computed values can be found in appendix B, Table B1. It should be noted that in the cases where Cd was placed at a Mn site, the systems were treated as ferromagnetic, for the sake of computational simplicity. An antiferromagnetic calculation for the  $\text{CaMn}_{7/8}\text{Cd}_{1/8}\text{Ge}_2\text{O}_6$  system was nevertheless performed to check how much of an effect the magnetic ordering might have on the computed EFG. Very similar results were obtained in both the ferromagnetic and antiferromagnetic calculations, with  $V_{zz}=12$  V/Å<sup>2</sup> and  $\eta=0.21$ , in the former case, and  $V_{zz}=13$  V/Å<sup>2</sup> and  $\eta=0.37$ , in the latter, thus showing that this approximation is reliable.

Comparing the EFG parameters for the experimental EFG<sup>SMGO1</sup> fraction of  $\text{SrMnGe}_2\text{O}_6$  with those computed

Table III. Experimental (highlighted in gray shaded cells, nomenclature as defined above in figures 5 and 3) and computational (absolute values) EFG parameters for  $\text{SrMnGe}_2\text{O}_6$  and  $\text{CaMnGe}_2\text{O}_6$  related compounds.

System	$ V_{zz} $ ( $\text{V}/\text{\AA}^2$ )	$\eta$
EFG <sup>SMGO1</sup> (13 K)	120(1)	0.28(1)
EFG <sup>SMGO2</sup> (13 K)	20(1)	0.81(6)
$\text{SrMnGe}_2\text{O}_6$ Sr-site	64	0.54
$\text{Sr}_{7/8}\text{Cd}_{1/8}\text{MnGe}_2\text{O}_6$	108	0.14
$\text{Sr}_{3/4}\text{Cd}_{1/4}\text{MnGe}_2\text{O}_6$	103	0.14
$\text{SrMnGe}_2\text{O}_6$ Mn-site	14	0.32
$\text{SrMn}_{7/8}\text{Cd}_{1/8}\text{Ge}_2\text{O}_6$	21	0.74
$\text{SrMn}_{3/4}\text{Cd}_{1/4}\text{Ge}_2\text{O}_6$	22	0.67
EFG <sup>CMGO1</sup> (11 K)	130(1)	0.15(1)
EFG <sup>CMGO2</sup> (351 K)	10(2)	—
$\text{CaMnGe}_2\text{O}_6$ Ca-site	34	0.52
$\text{Ca}_{7/8}\text{Cd}_{1/8}\text{MnGe}_2\text{O}_6$	109	0.01
$\text{Ca}_{3/4}\text{Cd}_{1/4}\text{MnGe}_2\text{O}_6$	108	0.02
$\text{CaMnGe}_2\text{O}_6$ Mn-site	8	0.49
$\text{CaMn}_{7/8}\text{Cd}_{1/8}\text{Ge}_2\text{O}_6$	12	0.21
$\text{CaMn}_{3/4}\text{Cd}_{1/4}\text{Ge}_2\text{O}_6$	12	0.31

for the supercells with Cd substitution at the Sr-site, where the 1/4 and 1/8 Cd dilution was considered (unit-cell and  $1 \times 1 \times 2$  supercell, respectively), we may observe a very good agreement between  $V_{zz}$  and  $\eta$ . From the PAC measurements we obtain for EFG<sup>SMGO1</sup> the values of  $V_{zz}=120 \text{ V}/\text{\AA}^2$  and  $\eta=0.28$ ; for the Cd probe nucleus for  $\text{Sr}_{3/4}\text{Cd}_{1/4}\text{MnGe}_2\text{O}_6$  they are  $V_{zz}=103 \text{ V}/\text{\AA}^2$  and  $\eta=0.14$  and for  $\text{Sr}_{7/8}\text{Cd}_{1/8}\text{MnGe}_2\text{O}_6$  these result as  $V_{zz}=108 \text{ V}/\text{\AA}^2$  and  $\eta=0.14$ . Likewise, good agreement is also observed for the EFG<sup>SMGO2</sup> fraction of  $\text{SrMnGe}_2\text{O}_6$  for the case of the Cd substitution at the Mn-site. We obtain for the EFG<sup>SMGO2</sup> fraction the values of  $V_{zz}=20 \text{ V}/\text{\AA}^2$  and  $\eta=0.81$ . From the DFT results we get  $V_{zz}=22 \text{ V}/\text{\AA}^2$  and  $\eta=0.67$ , and  $V_{zz}=21 \text{ V}/\text{\AA}^2$  and  $\eta=0.72$ , for the  $\text{SrMn}_{3/4}\text{Cd}_{1/4}\text{Ge}_2\text{O}_6$  and  $\text{SrMn}_{7/8}\text{Cd}_{1/8}\text{Ge}_2\text{O}_6$  cells, respectively. Based on the obtained theoretical results, we may conclude that the supercells are the systems that simulate quite well the experimental data when the Cd probe is considered, with the EFGs being in good agreement to the EFG<sup>SMGO1</sup> and EFG<sup>SMGO2</sup> experimental fractions, which correspond to the Cd probe replacing the Sr-sites and the Mn-sites, respectively, in the crystalline structure. Similarly, this same correspondence seems to hold true for the  $\text{CaMnGe}_2\text{O}_6$  compound. For the EFG<sup>CMGO1</sup> experimental fraction, we observe the values of  $V_{zz}=130 \text{ V}/\text{\AA}^2$  and  $\eta=0.15$ , and for the DFT data we obtain values of  $V_{zz}=108$  (109)  $\text{V}/\text{\AA}^2$  and  $\eta=0.01$  (0.02) for Cd concentration of 1/4 (1/8) in the Ca atom position. The obtained theoretical EFGs are slightly lower

than those of the experimental fraction; such is mostly evident for the asymmetry parameter,  $\eta$ . As for the EFG<sup>CMGO2</sup> fraction from the PAC experiments, the EFG result in  $V_{zz}=10 \text{ V}/\text{\AA}^2$  and an indeterminate  $\eta$ , whereas for the DFT diluted supercell of  $\text{CaMn}_{7/8}\text{Cd}_{1/8}\text{Ge}_2\text{O}_6$  we have  $V_{zz}=12 \text{ V}/\text{\AA}^2$  and  $\eta=0.21$ , similar to those obtained for  $\text{CaMn}_{3/4}\text{Cd}_{1/4}\text{Ge}_2\text{O}_6$ . These results indicate that first-principles calculations combined with PAC spectroscopy provide a valuable tool to explain the observed two distinct local environments, indicating that Cd probes are distributed between the Sr- or Ca-sites and the Mn-sites in the  $\text{SrMnGe}_2\text{O}_6$  and  $\text{CaMnGe}_2\text{O}_6$  basic compounds, respectively.

#### IV. CONCLUSIONS

We have undertaken DFT calculations to obtain the structural and electronic properties of the  $A\text{MnGe}_2\text{O}_6$  clinopyroxene systems, with  $A = \text{Be, Mg, Ca, Sr}$ . We found, through enthalpy of formation calculations, that the Be- and Mg-based systems are not thermodynamically stable against dissociation into the stable constituent oxides  $\text{BeGeO}_3$  or  $\text{MgGeO}_3$  and  $\text{MnGeO}_3$ . On the other hand, the Ca- and Sr-based systems are thermodynamically stable against dissociation and, accordingly, have been realized experimentally. From the PDOS, we found that the strongly correlated Mn  $3d$ -states form the narrow band close to the VBM together with the O  $p$ -states. The CBM is composed mainly of low density hybridized  $p$ -states of O and Ge and, for higher energies, the density of states significantly increases forming a narrow resonant band that is mainly composed of the anti-bound unoccupied Mn  $3d$ -states. The theoretical band gaps of  $\text{CaMnGe}_2\text{O}_6$  and  $\text{SrMnGe}_2\text{O}_6$  compounds, computed using the PBE+ $U$  approximation, are 1.82 eV and 1.70 eV, respectively. The calculated effective masses of the charge carriers of the two studied pristine compounds show considerable differences, which implies that the separation of the electron-hole pairs can be enhanced, thus improving the photoelectric efficiency. By considering the Cd dopants, we do not observe much variation on the value of the charge carrier masses, whereas a decrease of the band-gap widths is observed.

The temperature behavior of the experimental EFG  $V_{zz}$  fractions, labeled EFG<sup>SMGO1</sup> and EFG<sup>CMGO1</sup>, respectively related to the Cd probe on the  $\text{SrMnGe}_2\text{O}_6$  and  $\text{CaMnGe}_2\text{O}_6$  compounds, fits precisely, according to the Bayer-Kushida model [37–39], with a single phonon frequency, producing frequencies of  $8.01(7) \times 10^{12}$  and  $10.0(2) \times 10^{12}$  respectively, suggesting that their behavior can be attributed to a phonon contribution to  $V_{zz}$ .

The hyperfine parameters were computed to obtain the EFGs and these were compared to PAC measurement results. Data between both sets are consistent with the two obtained experimental fractions, EFG<sup>SMGO1</sup> and EFG<sup>SMGO2</sup>, when considering a supercell approach with a Cd ion replacing Sr and Mn sites, respectively. We

also find that this same correspondence seems to be true for the  $\text{CaMnGe}_2\text{O}_6$  compound, where the  $\text{EFG}^{\text{CMGO}_1}$  and  $\text{EFG}^{\text{CMGO}_2}$  experimental fractions can be attributed, respectively, to Cd replacing Ca and Mn ions. Furthermore, through the combination of theoretical *ab-initio* calculations and PAC results, we could infer that the Cd probe in the  $\text{AMnGe}_2\text{O}_6$  clinopyroxene compounds, with  $A = \text{Ca, Sr}$ , can replace the ion located at the A-site as well as the Mn ion, offering new perspectives for new systems synthesis with possibly improved functionalities.

## ACKNOWLEDGMENTS

The authors acknowledge the support of the technical teams at ISOLDE for their exceptional work in delivering high-quality beams for the presented PAC measurements. The authors also acknowledge project NECL under NORTE-01-0145-FEDER-022096, and FCT projects UIDP/04968/2020 (doi.org/10.54499/UIDP/04968/2020), UIDB/04968/2020 (doi.org/10.54499/UIDB/04968/2020), LaP-MET LA/P/0095/2020, POCI-01-0145-FEDER-029454, POCI-01-0145-FEDER-032527 and CERN/FIS-TEC/0003/2021. Also, BMBF through grants 05K16PGA and 05K22PGA, EU Horizon Europe Framework research and innovation programme under grant agreement no. 101057511 (EURO-LABS) for supporting IS679 ISOLDE-CERN experiment, and PRACE project with reference 2021240118, with access to the Irene Skylake computer. RPM acknowledges support from the Project HPC-EUROPA3 (INFRAIA-2016-1-730897), with the support of the EC Research Innovation Action under the H2020 Programme, with reference HPC171030W; in particular, the support of Dr. A. Stoppa and the hospitality provided by CNR-SPIN at the Department of Physical and Chemical Science of the University of L'Aquila (Italy) during the visit from 15/10/2021 to 20/12/2021 as well as computer resources and technical support provided by CINECA. RPM also acknowledges computer resources and technical support from Minho Advanced Computing Center through project CPCA/A1/460622/2021, financed by FCT. LVCA (Project 314884/2021-1) and HMP (Project 308438/2022-1) acknowledge funding from CNPq and support from FAPESP (Project 2022/10095-8). AMLL acknowledge the FCT 2021.04084.CEECIND (doi.org/10.54499/2021.04084.CEECIND/CP1655/CT0002) and ELdS the 2022.00082.CEECIND (doi.org/10.54499/2022.00082.CEECIND/CP1719/CT0001) grants. ELdS further acknowledges the High Performance Computing Chair - a R&D infrastructure (based at the University of Évora; PI: M. Avillez), endorsed by Hewlett Packard Enterprise, and involving a consortium of higher education institutions, research centers, enterprises, and public/private organizations.

Table A1. Electronic total energies of the  $\text{AMnGe}_2\text{O}_6$  clinopyroxene compounds ( $A = \text{Be, Mg, Ca, Sr}$ ) and their respective constituent  $\text{AGeO}_3$  and  $\text{MnGeO}_3$  oxides.

System	Energy (eV/f.u.)
$\text{SrMnGe}_2\text{O}_6$	-19433.62
$\text{CaMnGe}_2\text{O}_6$	-17709.36
$\text{MgMnGe}_2\text{O}_6$	-17815.41
$\text{BeMnGe}_2\text{O}_6$	-15984.00
$\text{SrGeO}_3$	-9540.40
$\text{CaGeO}_3$	-7816.06
$\text{MgGeO}_3$	-7922.42
$\text{BeGeO}_3$	-6091.01
$\text{MnGeO}_3$	-9893.11

## Appendix A: Calculation of Formation Energies

The formation energies for the studied oxides of the  $\text{AMnGe}_2\text{O}_6$  ( $A = \text{Be, Mg, Ca, Sr}$ ) clinopyroxene series, were calculated according to the following equation:

$$E_{\text{form}} = E_{\text{AMnGe}_2\text{O}_6} - E_{\text{AGeO}_3} - E_{\text{MnGeO}_3}, \quad (\text{A1})$$

where  $E_{\text{AMnGe}_2\text{O}_6}$ ,  $E_{\text{AGeO}_3}$ ,  $E_{\text{MnGeO}_3}$  are the total electronic energies obtained from DFT+ $U$  calculations, per formula unit (f.u.), which are summarised in table A1.

## Appendix B: Electric Field Gradient Parameters

The calculated EFG parameters are presented in table B1. From these results we can observe that the EFGs at the Ge nuclei were only slightly affected by the Cd substitution, as evidenced by the fact that the symmetry of the Ge sites remained quite similar to  $\text{SrMnGe}_2\text{O}_6$  and  $\text{CaMnGe}_2\text{O}_6$  basic compounds after Cd substitution. The same cannot be said for the Sr/Ca and Mn sites, which in many cases deviated substantially.

## Appendix C: Electronic Band Dispersion of the Cd Doped Systems

The bandstructure and the density of states for the  $\text{AMnGe}_2\text{O}_6$  ( $A = \text{Ca, Sr}$ ) clinopyroxene compounds with Cd substitution in A- and Mn-sites are presented in figures C1 to C9.

Table B1. Computational EFG parameters at the Sr, Ca, Mn, Ge, and Cd nuclei for  $\text{SrMnGe}_2\text{O}_6$ ,  $\text{SrMnGe}_2\text{O}_6:\text{Cd}_{\text{Sr}}$ , and  $\text{SrMnGe}_2\text{O}_6:\text{Cd}_{\text{Mn}}$  compounds, and for  $\text{CaMnGe}_2\text{O}_6$ ,  $\text{CaMnGe}_2\text{O}_6:\text{Cd}_{\text{Ca}}$ , and  $\text{SrMnGe}_2\text{O}_6:\text{Cd}_{\text{Mn}}$  compounds.

System	EFG	Cd	Sr(1)	Sr(2)	Sr(3)	Sr(4)	Mn(1)	Mn(2)	Mn(3)	Mn(4)	Ge(1)	Ge(2)	Ge(3)	Ge(4)
$\text{SrMnGe}_2\text{O}_6$	$ V_{zz} $ ( $\text{V}/\text{\AA}^2$ )	-	64	-	-	-	14	-	-	-	99	-	-	-
	$\eta$	-	0.54	-	-	-	0.32	-	-	-	0.70	-	-	-
$\text{Sr}_{7/8}\text{Cd}_{1/8}\text{MnGe}_2\text{O}_6$	$ V_{zz} $	108	61	62	63	66	10	19	17	12	101	97	102	101
	$\eta$	0.14	0.46	0.71	0.53	0.83	0.64	0.98	0.44	0.84	0.60	0.64	0.64	0.69
$\text{Sr}_{3/4}\text{Cd}_{1/4}\text{MnGe}_2\text{O}_6$	$ V_{zz} $	103	59	65	64	-	19	17	14	15	99	103	91	85
	$\eta$	0.14	0.88	0.82	0.66	-	0.42	0.75	0.60	0.16	0.55	0.64	0.55	0.67
$\text{SrMn}_{7/8}\text{Cd}_{1/8}\text{Ge}_2\text{O}_6$	$ V_{zz} $	21	57	67	64	68	14	14	11	14	99	99	101	100
	$\eta$	0.74	0.47	0.63	0.57	0.59	0.28	0.46	0.63	0.35	0.71	0.69	0.69	0.69
$\text{SrMn}_{3/4}\text{Cd}_{1/4}\text{Ge}_2\text{O}_6$	$ V_{zz} $	22	59	64	69	66	15	10	15	-	99	101	100	102
	$\eta$	0.67	0.56	0.59	0.63	0.64	0.58	0.61	0.23	-	0.71	0.67	0.73	0.69
System	EFG	Cd	Ca(1)	Ca(2)	Ca(3)	Ca(4)	Mn(1)	Mn(2)	Mn(3)	Mn(4)	Ge(1)	Ge(2)	Ge(3)	Ge(4)
$\text{CaMnGe}_2\text{O}_6$	$ V_{zz} $	-	34	-	-	-	8	-	-	-	96	-	-	-
	$\eta$	-	0.52	-	-	-	0.49	-	-	-	0.64	-	-	-
$\text{Ca}_{7/8}\text{Cd}_{1/8}\text{MnGe}_2\text{O}_6$	$ V_{zz} $	109	33	35	34	38	5	8	11	9	99	97	98	99
	$\eta$	0.01	0.45	0.34	0.45	0.33	0.43	0.30	0.69	0.93	0.52	0.60	0.60	0.60
$\text{Ca}_{3/4}\text{Cd}_{1/4}\text{MnGe}_2\text{O}_6$	$ V_{zz} $	108	35	38	35	-	2	12	11	8	99	100	96	86
	$\eta$	0.02	0.13	0.27	0.29	-	0.09	0.11	0.15	0.95	0.50	0.58	0.44	0.67
$\text{CaMn}_{7/8}\text{Cd}_{1/8}\text{Ge}_2\text{O}_6$	$ V_{zz} $	12	30	37	36	36	7	7	10	7	98	97	99	97
	$\eta$	0.21	0.42	0.41	0.38	0.39	0.76	0.92	0.34	0.82	0.63	0.61	0.60	0.66
$\text{CaMn}_{3/4}\text{Cd}_{1/4}\text{Ge}_2\text{O}_6$	$ V_{zz} $	12	31	37	38	37	7	10	8	-	97	99	98	100
	$\eta$	0.31	0.42	0.39	0.40	0.39	0.37	0.38	0.96	-	0.63	0.58	0.64	0.59

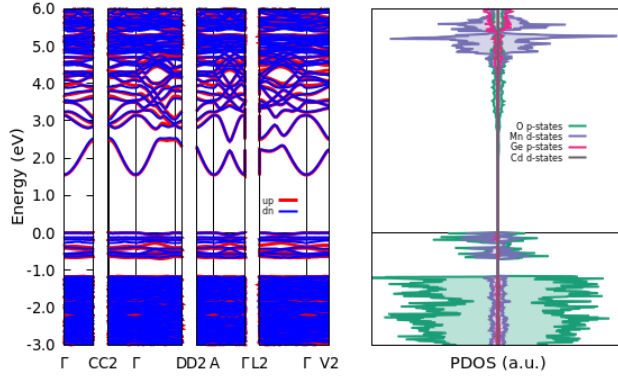


Figure C1. Electronic bandstructure (left) and density of states (right) for  $\text{Sr}_{7/8}\text{Cd}_{1/8}\text{MnGe}_2\text{O}_6$  with antiferromagnetic ordering.

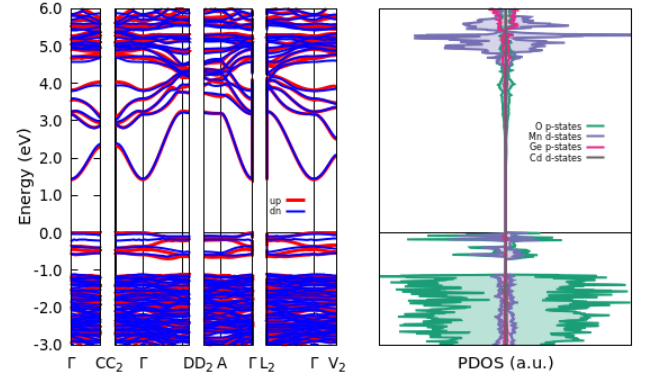


Figure C2. Electronic bandstructure (left) and density of states (right) for  $\text{Sr}_{3/4}\text{Cd}_{1/4}\text{MnGe}_2\text{O}_6$  with antiferromagnetic ordering.



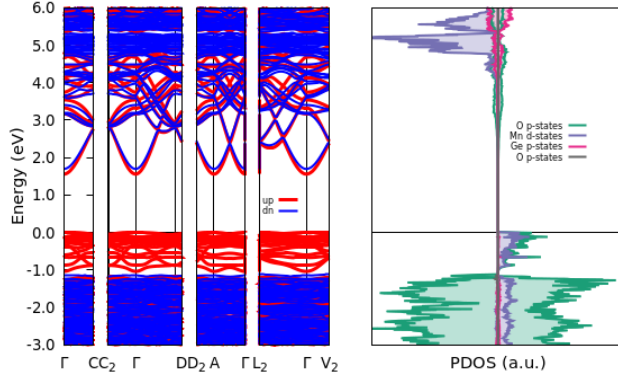


Figure C3. Electronic bandstructure (left) and density of states (right) for  $\text{SrMn}_{7/8}\text{Cd}_{1/8}\text{Ge}_2\text{O}_6$  with ferromagnetic ordering.

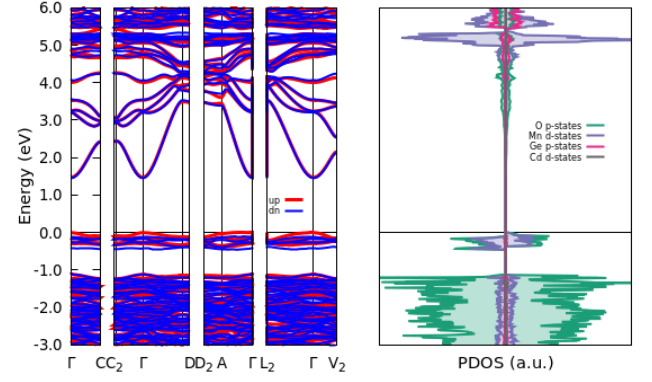


Figure C6. Electronic bandstructure (left) and density of states (right) for  $\text{Ca}_{3/4}\text{Cd}_{1/4}\text{MnGe}_2\text{O}_6$  with antiferromagnetic ordering.

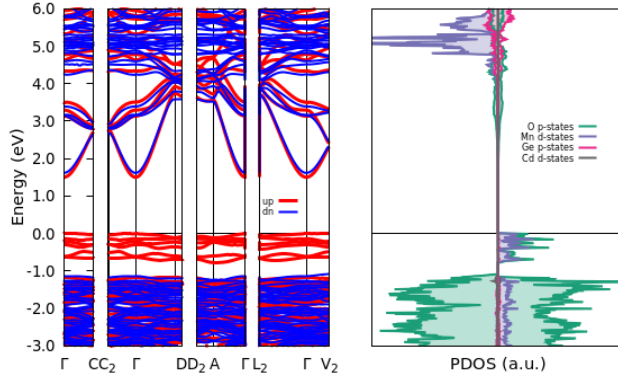


Figure C4. Electronic bandstructure (left) and density of states (right) for  $\text{SrMn}_{3/4}\text{Cd}_{1/4}\text{Ge}_2\text{O}_6$  with ferromagnetic ordering.

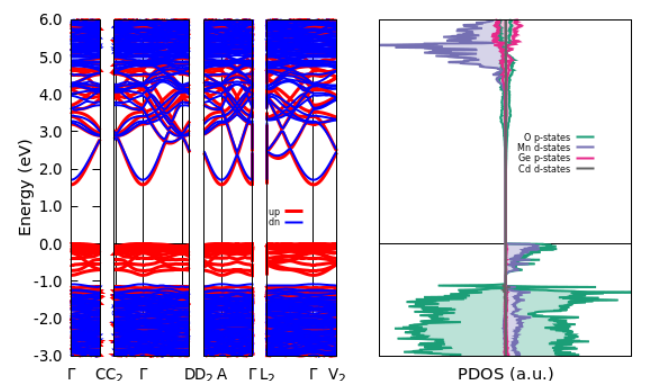


Figure C7. Electronic bandstructure (left) and density of states (right) for  $\text{CaMn}_{7/8}\text{Cd}_{1/8}\text{Ge}_2\text{O}_6$  with ferromagnetic ordering.

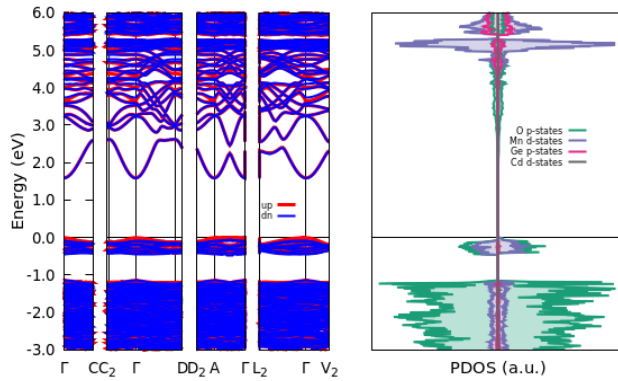


Figure C5. Electronic bandstructure (left) and density of states (right) for  $\text{Ca}_{7/8}\text{Cd}_{1/8}\text{MnGe}_2\text{O}_6$  with antiferromagnetic ordering.

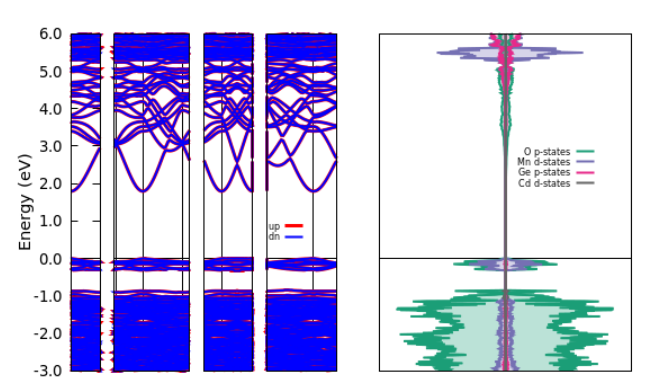


Figure C8. Electronic bandstructure and density of states for  $\text{CaMn}_{3/4}\text{Cd}_{1/4}\text{Ge}_2\text{O}_6$  with antiferromagnetic ordering.

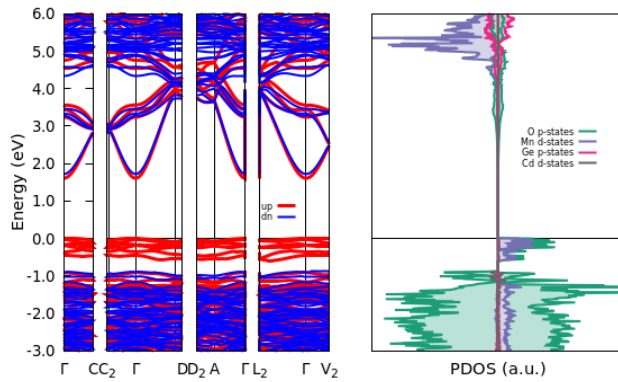


Figure C9. Electronic bandstructure (left) and density of states (right) for  $\text{CaMn}_{3/4}\text{Cd}_{1/4}\text{Ge}_2\text{O}_6$  with ferromagnetic ordering.

- 
- [1] S. V. Streltsov and D. I. Khomskii, *Phys. Rev. B* **77**, 064405 (2008).
- [2] L. Ding, C. V. Colin, C. Darie, and P. Bordet, *J. Mater. Chem. C* **4**, 4236 (2016).
- [3] C. V. Colin, L. Ding, E. Ressouche, J. Robert, N. Terada, F. Gay, P. Lejay, V. Simonet, C. Darie, P. Bordet, et al., *Phys. Rev. B* **101**, 235109 (2020).
- [4] S. Jodlauk, P. Becker, J. A. Mydosh, D. I. Khomskii, T. Lorenz, S. V. Streltsov, D. C. Hezel, and L. Bohatý, *J. Phys. Condens. Matter* **19**, 432201 (2007).
- [5] I. Kim, B.-G. Jeon, D. Patil, S. Patil, G. Nénert, and K. H. Kim, *J. Phys. Condens. Matter* **24**, 306001 (2012).
- [6] L. Ding, C. V. Colin, C. Darie, J. Robert, F. Gay, and P. Bordet, *Phys. Rev. B* **93**, 064423 (2016).
- [7] M. Legesse, H. Park, F. El Mellouhi, S. N. Rashkeev, S. Kais, and F. H. Alharbi, *Chem. Phys. Chem.* **19**, 943 (2018).
- [8] A. Torres, F. J. Luque, J. Tortajada, and M. E. Arroyo-de Dompablo, *Sci. Rep.* **9**, 9644 (2019).
- [9] S. Zhou, G. King, D. O. Scanlon, M. T. Sougrati, and B. C. Melot, *J. Electrochem. Soc.* **161**, A1642 (2014).
- [10] F. V. Temnikov, E. V. Komleva, Z. V. Pchelkina, and S. V. Streltsov, *JETP Lett.* **110**, 595 (2019).
- [11] S. E. Ashbrook, A. J. Berry, and S. Wimperis, *J. Phys. Chem. B* **106**, 773 (2002).
- [12] R. L. Flemming and R. W. Luth, *Am. Mineral.* **87**, 25 (2002).
- [13] K. Begaudeau, Y. Morizet, P. Florian, M. Paris, and J.-C. Mercier, *Eur. J. Mineral.* **24**, 535 (2012).
- [14] E. Dowty and D. H. Lindsley, *Am. Mineral.* **58**, 850 (1973).
- [15] M. D. Dyar, R. L. Klima, A. Fleagle, and S. E. Peel, *Am. Mineral.* **98**, 1172 (2013).
- [16] M. I. Oshtrakh, E. V. Petrova, V. I. Grokhovsky, and V. A. Semionkin, *Hyperfine Interact.* **177**, 65 (2007).
- [17] P. Raghavan, *At. Data Nucl. Data Tables* **42**, 189 (1989).
- [18] T. Butz, *Hyperfine Interact.* **52**, 189 (1989).
- [19] G. Schatz and A. Weidinger, *Nuclear condensed matter physics : nuclear methods and applications* (John Wiley, 1996), ISBN 9780471954798.
- [20] A. M. L. Lopes, J. P. Araújo, J. J. Ramasco, V. S. Amaral, R. Suryanarayanan, and J. G. Correia, *Phys. Rev. B* **73**, 100408 (2006).
- [21] N. P. Barradas, M. Rots, A. A. Melo, and J. C. Soares, *Phys. Rev. B* **47**, 8763 (1993).
- [22] J. G. Correia, *Nnfit the pac manual* (1992).
- [23] J. G. Correia, *Nnfit and fft upgrades 2018* (2018).
- [24] R. L. Rasera and G. L. Catchen, *Ferroelectr.* **150**, 151 (1993).
- [25] P. Giannozzi, S. Baroni, N. Bonini, M. Calandra, R. Car, C. Cavazzoni, D. Ceresoli, G. L. Chiarotti, M. Cococcioni, I. Dabo, et al., *J. Phys. Condens. Matter* **21**, 395502 (2009).
- [26] P. Giannozzi, O. Andreussi, T. Brumme, O. Bunau, M. B. Nardelli, M. Calandra, R. Car, C. Cavazzoni, D. Ceresoli, M. Cococcioni, et al., *J. Phys. Condens. Matter* **29**, 465901 (2017).
- [27] P. E. Blöchl, *Phys. Rev. B* **50**, 17953 (1994).
- [28] A. Dal Corso, *Comput. Mater. Sci.* **95**, 337 (2014).
- [29] J. P. Perdew, K. Burke, and M. Ernzerhof, *Phys. Rev. Lett.* **77**, 3865 (1996).
- [30] Data retrieved from the Materials Project for  $\text{SrMn}(\text{GeO}_3)_2$  (mp-1208680) from database version v2022.10.28..
- [31] A. Jain, S. P. Ong, G. Hautier, W. Chen, W. D. Richards, S. Dacek, S. Cholia, D. Gunter, D. Skinner, G. Ceder, et al., *APL Mater.* **1**, 011002 (2013).
- [32] M. Cococcioni and S. de Gironcoli, *Phys. Rev. B* **71**, 035105 (2005).
- [33] R. M. Wentzcovitch, *Phys. Rev. B* **44**, 2358 (1991).
- [34] J. H. Kim, K. Levin, R. Wentzcovitch, and A. Auerbach, *Phys. Rev. B* **44**, 5148 (1991).
- [35] R. M. Wentzcovitch, J. L. Martins, and G. D. Price, *Phys. Rev. Lett.* **70**, 3947 (1993).

- [36] T. Charpentier, Solid State Nucl. Magn. Reson. **40**, 1 (2011).
- [37] H. Bayer, Z. Phys. **130**, 227 (1951).
- [38] T. Kushida, J. Sci. Hiroshima Univ., Ser. A **19**, 327 (1955).
- [39] T. Kushida, G. Benedek, and N. Bloembergen, Phys. Rev. **104**, 1364 (1956).
- [40] P. Rocha-Rodrigues, S. S. M. Santos, G. m. c. N. P. Oliveira, T. Leal, I. P. Miranda, A. M. dos Santos, J. a. G. Correia, L. V. C. Assali, H. M. Petrilli, J. a. P. Araújo, et al., Phys. Rev. B **102**, 104115 (2020).
- [41] P. Rocha-Rodrigues, S. S. M. Santos, I. P. Miranda, G. N. P. Oliveira, J. G. Correia, L. V. C. Assali, H. M. Petrilli, J. P. Araújo, and A. M. L. Lopes, Phys. Rev. B **101**, 064103 (2020).
- [42] P. Haas, F. Tran, and P. Blaha, Phys. Rev. B **79**, 085104 (2009).
- [43] S. V. Streltsov, J. McLeod, A. Moewes, G. J. Redhammer, and E. Z. Kurmaev, Phys. Rev. B **81**, 045118 (2010).
- [44] Y. Hinuma, G. Pizzi, Y. Kumagai, F. Oba, and I. Tanaka, Computational Materials Science **128**, 140 (2017), ISSN 0927-0256.
- [45] A. Togo, K. Shinohara, and I. Tanaka, *Spglib: a software library for crystal symmetry search* (2024), 1808.01590.
- [46] Comput. Mater. Sci. **123**, 1 (2016).
- [47] E. Y. Lee, R. B. James, R. Olsen, and H. Hermon, J. Electron. Mater. **28**, 766 (1999).
- [48] J.-R. Zhang, X.-Z. Deng, B. Gao, L. Chen, C.-T. Au, K. Li, S.-F. Yin, and M.-Q. Cai, Catal. Sci. Technol. **9**, 4659 (2019).